Full-field strain analysis of bone-biomaterial systems produced by the implantation of osteoregenerative biomaterials in an ovine model

Marta Peña Fernández[1], Enrico Dall'Ara[2], Andrew J. Bodey[3], Rachna Parwani[1], Asa H. Barber[1,4], Gordon W. Blunn[5], Gianluca Tozzi[1]*

Affiliations:

1. Zeiss Global Centre, School of Mechanical and Design Engineering, University of Portsmouth, Anglesea Building, Anglesea Road, Portsmouth, PO1 3DJ, UK.

2. Department of Oncology and Metabolism and INSIGNEO institute for *in silico* medicine, University of Sheffield, The Pam Liversidge Building, Sir Robert Hadfield Building, Mappin Street, Sheffield, S1 3JD, UK.

3. Diamond Light Source, Diamond House, Harwell Science and Innovation Campus, Fermi Avenue, Didcot, OX11 0DE, UK.

4. School of Engineering, London South Bank University, 103 Borough Road, London, SE1 0AA UK.

5. School of Pharmacy and Biomedical Sciences, University of Portsmouth, Portsmouth, St Michael's Building, White Swan Road, Portsmouth, PO1 2DT, UK.

*Corresponding author:

Dr Gianluca Tozzi

School of Mechanical and Design Engineering, University of Portsmouth

Anglesea Building, Anglesea Road

PO1 3DJ, Portsmouth

United Kingdom

Tel: +44 (0)239284 2514

Email: gianluca.tozzi@port.ac.uk

ABSTRACT

Osteoregenerative biomaterials for the treatment of bone defects are under much development, with the aim of favouring osteointegration up to complete bone regeneration. A detailed investigation of bone-biomaterial integration is vital to understanding and predicting the ability of such materials to promote bone formation, preventing further bone damage and supporting load-bearing regions. This study aims to characterise the *ex vivo* micromechanics and microdamage evolution of bone-biomaterial systems at the tissue level, combining high resolution synchrotron micro-computed tomography, *in situ* mechanics and digital volume correlation. Results showed that the main microfailure events were localised close to or within the newly formed bone tissue, in proximity to the bone-biomaterial interface. The apparent nominal compressive load applied to the composite structures resulted in a complex loading scenario, mainly due to the higher heterogeneity but also to the different biomaterial degradation mechanisms. The full-field strain distribution allowed characterisation of microdamage initiation and progression. The findings reported in this study provide a deeper insight into bone-biomaterial integration and micromechanics in relation to the osteoregeneration achieved *in vivo*, for a variety of biomaterials. This could ultimately be used to improve bone tissue regeneration strategies.

KEYWORDS

Osteoregenerative biomaterials, bone-biomaterial interface, SR-microCT, *in situ* mechanics, digital volume correlation.

1. INTRODUCTION

Bone is constantly undergoing remodelling during life due to the necessity of adapting to loading conditions and to remove old damaged bone, replacing it with new, mechanical stronger tissue; thus preserving bone strength [1]. As a dynamically adaptable material, bone displays excellent regenerative properties [2]; however, non-union fractures, tumour resections and some musculoskeletal diseases can lead to critical size bone defects [3], which cannot heal spontaneously and require additional treatments before they can regenerate [4]. Bone is the second most frequent transplanted tissue after blood transfusion [5]. It is estimated that over two million bone grafting procedures are performed annually worldwide [6] aiming at augmenting bone formation. Current strategies for bone grafts include the use of autografts, allografts and synthetic grafts. Although autografting is still considered as the gold standard [7–9] for stimulating bone repair and regeneration, it is accompanied with risks of donor site morbidity and limited availability [10,11]. Even though the use of allografts, taken from cadavers or donors, circumvent some of the shortcomings of autografts, the procedure is limited by risk of transmission of disease and a high non-union rate with the host tissue [12,13]. The development of synthetic bone substitutes during the past decades has provided a valuable alternative, addressing the limitations of autologous and allogeneic bone grafts and improving bone regeneration by incorporating osteoconductive properties [7,14–16]. Among those synthetic materials, calcium phosphate ceramics and bioactive glasses are widely used in reconstruction of large bone defects [7,17,18].

Calcium phosphates ceramics (CPCs) are constituted by calcium hydroxyapatite (HA), which is similar in chemical composition to the mineral phase of bone [19]. The composition of the final product can be controlled by adjusting the calcium/phosphate ratio (Ca/P). Among CPCs, HA-based ceramics show excellent osteoconductive and osteointegrative properties [17,19]. Therefore, they have gained great attention in clinical studies [20–24]. However, their relative high Ca/P ratio

and crystallinity delay the resorption rate of HA, which typically exhibit a slow resorption at the early stages (weeks 1 to 6) and require long times (months to years) for a complete integration *in vivo* and subsequent replacement by newly formed bone [17]. Conversely, bioactive glass refers to a group of synthetic silicate-based ceramics, characterized mainly by their osteoconductive properties, but they also present some osteoinductivity [25–27]. Bioactive glasses are composed of silicate, sodium oxide, calcium oxide, and phosphorous pentoxide; the key component, silicate, constitutes 45-52% of its weight. This optimised constitution lead to a strong and rapid bonding to bone tissue [28,29]. Additionally, they show a fast resorption rate in the first weeks of implantation and can be completely resorbed within six months [18]. Bioactive glass materials are widely used clinically to repair bone defects in maxillofacial and orthopaedic interventions [27,30].

Bone defect animal models remain essential tools for preclinical research of novel biomaterials [31,32], overcoming limitations of *in vitro* studies due to the reduced complexity of the environment. Appropriate *in vivo* bone healing models for assessment of bone substitutes materials under different loading conditions; for extended duration, in different tissue qualities and age [32,33]. Therefore, the establishment of a suitable animal model is essential prior to the evaluation of novel biomaterials. The use of ovine models to test new bone grafts has increased over time because of their similarities with humans in weight, bone structure and bone regeneration [34–37]. Typically, defects are created in a weight-bearing region of the sheep bone, which provides similarities in bone composition, defect size and healing rate compared to humans [36,38]. Critical defects models generally evaluate the *in vivo* performance of biomaterials in terms of bone regeneration, remodelling, biomaterial resorption and biological effects [35,39,40]. However, their biomechanical competence after implantation is poorly understood [41]. A micromechanical characterisation of the bone-biomaterial systems produced *in vivo* after different bone grafting procedures is essential to demonstrate their ability to produce bone that

is comparable with the native tissue they are meant to replace, and therefore, support load-bearing regions. More specifically, an understanding of the internal microdamage progression at the bone-biomaterial interface, which could promote the failure of the entire bone structure, is needed to further characterise the mechanical performance and overall structural response of such composites.

A combination of time-lapsed micro-computed tomography (microCT) with *in situ* mechanics allows the evaluation of the internal microdamage progression in bone and biomaterials [42,43]. Furthermore, a quantification of full-field strain field can be achieved using digital volume correlation (DVC). In fact, during the past decade DVC has become a powerful and unique tool to examine the three-dimensional (3D) internal deformations in bone [44–46] and bone-biomaterial composites [47,48]. Particularly, Tozzi et al. [47] assessed the microdamage of bone-cement interfaces under monotonic and cyclic compression, and more recently, Danesi el al. [48] applied DVC to study failure mechanisms of cement-augmented vertebral bodies. Both studies successfully showed the internal strain distribution in bone-biomaterial composites under different loading scenarios, however some questions remain. Firstly, bone-cement composites were produced *in vitro*, restricting the real integration of both materials, and therefore the *in vivo* competence. In addition, strain measurements were computed at the apparent level, enabling the classification of high- or lowly localised strains in relatively large regions (above 0.6 mm); thus, unable to provide information of the strain distribution at the interface and in the tissue. Actually, deformation mechanisms at the bone-biomaterial interfaces are still missing due to the intrinsic limitation of laboratory-based microCT systems, which are unable to offer sufficient spatial resolution and signal to noise ratio (SNR) to properly resolve features at the boundary without the requirement of long acquisitions times. This problem can be overcome using synchrotron radiation (SR) based microCT, to access fast imaging with high spatial resolution and SNR [49–51]. Additionally, DVC based on SR-microCT images has recently

been proven to provide reliable strain measurements at the tissue level [52–54], suggesting that an accurate 3D full-field strain evaluation can be obtained at bone-biomaterial interfaces [55].

The main purpose of this study was to investigate, for the first time, the 3D full-field strain distribution at the bone-biomaterial interface, in relation to the newly regenerated bone produced *in vivo* after the implantation of commercial osteoregenerative grafts in an ovine model. DVC in conjunction with *in situ* SR-microCT mechanics was performed to evaluate the internal strain and microdamage evolution of bone-biomaterial systems under compression. The finding of this paper will improve the understanding of the micromechanical behaviour of bone-biomaterial structures formed *in vivo* due to the bone regeneration process associated with bone grafting procedures.

2. METHODS

2.1. Biomaterials

Cylindrical bone defects (8 mm diameter by 14 mm depth) were surgically created [56] in the femoral condyles of a female adult sheep (80 Kg). Four different synthetic bone graft materials were then implanted in the defects under Ethics approval granted by the Royal Veterinary College and in compliance with the United Kingdom Home Office regulations (Animal Scientific Procedure Act [1986]).

The selected bone graft materials are commercially available biomaterials: Actifuse; ApaPore (ApaTech Ltd, UK); StronBone and StronBone-P (RepRegen Ltd, UK). Actifuse and ApaPore are HA-based bioceramics. Whereas ApaPore presents a pure HA phase, Actifuse is a silicon-substituted HA (Si-HA), containing 0.8% silicon by weight [57]. Both materials have an interconnected macro and microporous structure, which favours the scaffold osteoconduction. Additionally, the incorporation of silicon to the bone graft promotes rapid bone formation [58]. StronBone and StronBone-P are silicate-based bioactive glasses containing strontium, which has shown a positive effect on bone metabolism [27]. StronBone-P is a more porous version of

StronBone and has been proven to promote a more rapid bone growth and higher remodelling rate [59]. The choice of four different biomaterials was intended at exploring microdamage mechanisms at the bone-biomaterial interface, in relation to their different osteointegration and osteoconduction performance on the same animal model following *in vivo* service.

2.2. MicroCT scanning and sample preparation

Six weeks after implantation, both left and right condyles were harvested. X-ray micro-computed tomography (microCT) was conducted (ZEISS Xradia Versa 520) using a flat panel detector to identify areas of bone and biomaterial, as shown in Figure 1. Condyles were kept immersed in saline solution throughout image acquisition. The instrument was set to a voltage of 110 kV and a current of 91 µA. With an isotropic effective voxel size of 56 µm, 2001 projections were acquired over 360° with an exposure time of 0.36 s per projection. After inspection of the reconstructed microCT images, the desired sample locations were identified (Figure 1) and a trephine blur drill was manually positioned following the condyle and defect geometry. Cylindrical samples (4 mm in diameter and 18 mm in length) were then cored from the thawed condyles in the proximal-distal direction (Figure 1). The biomaterial regions were clearly visible in the condyles; however, the amount and position of the graft within each bone-biomaterial system could not be controlled during the extraction. Such difficulties allowed for only four bone-biomaterial systems from the bone defect areas to be extracted; additionally, one control sample (trabecular bone) was also cored (Figure 2). The ends of the cores were trimmed plane and parallel, and end-constraint was achieved by embedding the samples in poly-methyl-methacrylate (PMMA) endcaps. Approximately 5 mm of the core was embedded into each endcap to achieve a 2:1 aspect ratio, reducing experimental artifacts [60] during mechanical testing. Samples were kept frozen at -20° and thawed for around 2 h in saline solution at room temperature before image acquisition.

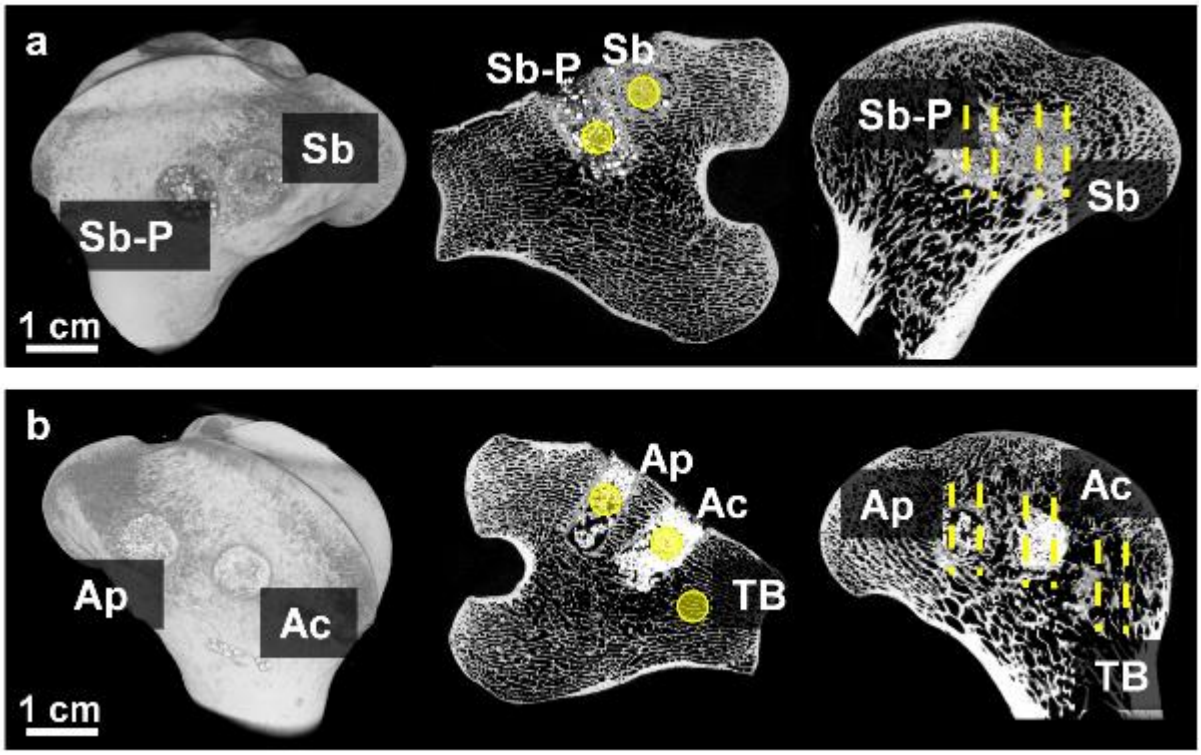

Figure 1. 3D volume reconstruction (left) and representative microCT slices of the four bone defects in the left (a) and right (b) femoral condyles, showing osteointegration of the bone grafts. (Ac: Actifuse; Ap: ApaPore; Sb: StronBone, Sb-P: StronBone-P, TB: Trabecular bone control). Sites of sample extraction are marked with yellow circles (middle figures), whilst direction of extraction is marked with dashed lines (right figures).

2.3. SR-microCT and in situ mechanics

SR-microCT imaging was performed at the Diamond-Manchester Imaging Branchline I13-2 (Diamond Light Source, UK), using a filtered (1.3 mm pyrolytic graphite, 3.2 mm aluminium and 60µm steel), partially-coherent, polychromatic 'pink' beam (5-35 keV) of near-parallel geometry with an undulator gap of 5 mm. Samples were aligned for imaging under low-dose conditions (~10 minutes per sample) by temporarily setting the undulator gap to 10 mm [61]. Projections were recorded by a sCMOS (2560 x 2160 pixels) pco.edge 5.5 (PCO AG, Germany) detector, which was coupled to a visual light microscope. A 1.25X objective lens (with 500 µm-thick $CdWO_4$ scintillator) was used to achieve a total magnification of 2.5X,

resulting in an effective voxel size of 2.6 µm and a field of view of 6.7 x 5.6 mm. For each dataset, 1801 projection images were collected over 180 degrees of continuous rotation ('fly scan'). The exposure time was set to 64 ms per projection in order to minimise irradiation-induced damage during image acquisition [62]. The propagation distance (sample to detector) was set to 150 mm to provide sufficient in-line phase contrast and better visualise the microstructure [55]. The projection images were flat-field and dark-field corrected prior to reconstruction. For each dataset, 40 flat and dark images were collected. Reconstruction was performed at Diamond using the in-house software, DAWN [63,64], incorporating ring artefact suppression.

In situ uniaxial compression testing was performed using a micro-mechanical loading stage equipped with a 5kN load cell and environmental chamber (CT5000, Deben Ltd, UK). Specimens were immersed in saline solution throughout the duration of the test to simulate physiological conditions. A small preload (~5N) was first applied to ensure good end contact prior to testing. Each specimen was subjected to four compression steps under displacement control at a constant cross-head speed of 0.1 mm/min. The first three compression steps were set to 0.1, 0.25 and 0.5 mm of displacement, whereas for the last step the actuator was stopped after failure detection from the load-displacement curve. Specimens were allowed to settle for 10 minutes after each compression step before image acquisition to reduce stress relaxation during imaging. Full tomographic datasets were acquired at each loading step, under the applied displacement, after two repeated scans (preload state) prior to loading for DVC error analysis [52].

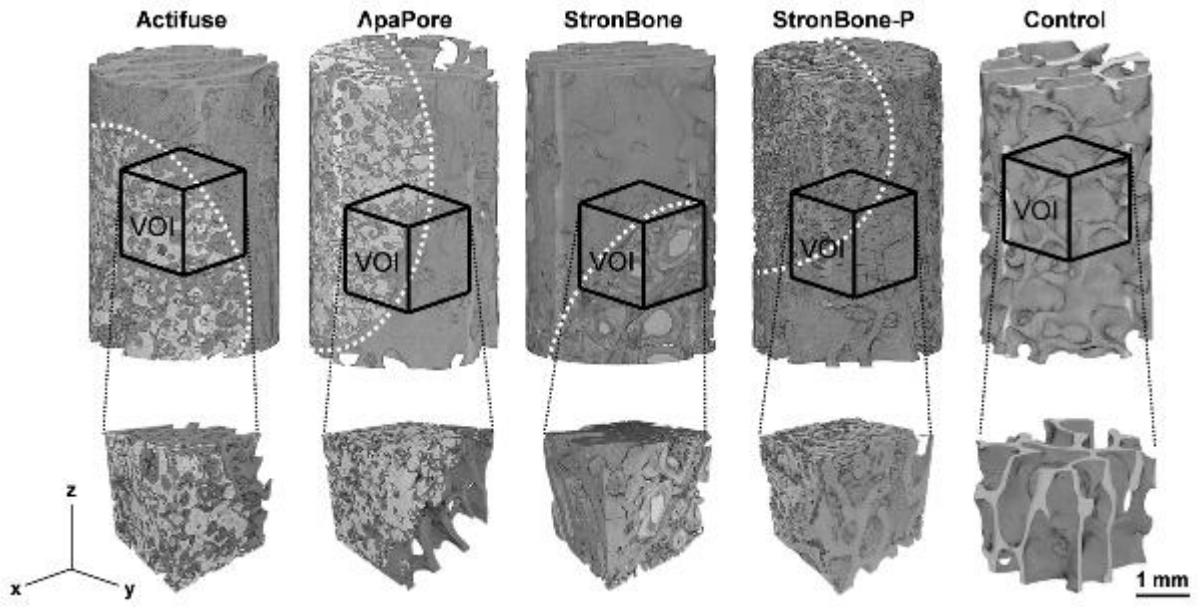

Figure 2. SR-microCT reconstruction of the four cylindrical bone-biomaterial systems and the trabecular bone control sample (4 mm in diameter and 5.6 mm in height) showing the cubic volume of interest (VOI, 2.6 mm^3) used for DVC analysis. VOIs were selected to include the interface (dotted white line) between the different grafts and the bone tissue. Samples were compressed in the z direction.

2.4. Image post-processing

After image acquisition, the 3D datasets were rigidly registered using the unloaded image as a reference [55]. Then, images were denoised by applying a non-local means filter [65,66]. The filtered SR-microCT images were masked by setting to zero the grayscale intensity of non-bone/biomaterial voxels [55]. Briefly, binary images (value one for bone-biomaterial voxels and zero elsewhere) were created using a global thresholding segmentation followed by an iterative approach that filled small holes and removed isolated pixels. Masked images were obtained by multiplying the filtered and binary 3D images. The same approach was used to segment the remaining bone graft from the bone tissue in bone-Actifuse, bone-ApaPore and bone-StronBone-P specimens. This procedure could not be applied to the bone-StronBone as the biomaterial was considerably more resorbed and the difference in the grey-level intensity

between bone and biomaterial was minimal (Figure 2). The solid volume fraction (SV/TV) was computed for each specimen as the amount of material in the hard phase (bone/biomaterial) over the total volume (TV) of the imaged specimens. Additionally, the bone volume fraction (BV/TV) and graft volume fraction (GV/TV) were similarly computed for the bone-Actifuse, bone-ApaPore and bone-StronBone-P specimens. Finally, a volume of interest (VOI) was cropped from each tomogram for DVC analysis. The VOI consisted of a parallelepiped with side lengths of 1000 voxels (2.6 mm^3) and it was set in the centre of the volume for the trabecular bone specimen (control) and manually selected for the bone-biomaterial specimens in order to include the bone-biomaterial interface (Figure 2).

2.5. Digital volume correlation

DVC (DaVis v8.4, LaVision, Goettingen, Germany) was used to compute full-field strains throughout the bone-biomaterial composites and the control trabecular bone specimens after each compression step. DaVis is a cross-correlation method operating on the intensity values (grey-level) of 3D images. The operating principles have been extensively reported elsewhere [55,67]. The DVC parameters used in this study relied on a previous methodological work based on repeated SR-microCT scans of the specimens in a 'zero-strain' condition for the error assessment as a function of sub-volume size and imaging post-processing [55].

Thus, DVC computation was conducted using a multi-pass scheme [67] with a final sub-volume of 48 voxels, reached via successive (predictor) passes using sub-volumes of 112, 96, 80 and 64 voxels, with 0% overlap between the sub-volumes. DVC was applied to the masked images, treating the non-hard phase as a black 'zero-count' region to avoid large strain artifacts in regions without a clear pattern distribution (i.e. saline, bone marrow). Additionally, sub-volumes with a correlation coefficient below 0.6 were removed from the resultant vector, to avoid artifacts due to poor correlation. Errors on the DVC-computed displacements using the described settings did not exceed 0.22 µm, whereas the mean absolute error (MAER) and the

standard deviation of the error (SDER) of the strain components were found to be ~200 με and ~100 με, respectively. Given the voxel size of the SR-microCT images, the final DVC computed spatial resolution corresponded to ~125 μm; thus, providing full-field strain at the tissue level, within the bone tissue and/or biomaterial [52,55].

In order to evaluate the 3D full-field strain distribution in the selected specimens over time in relation to the deformation induced by the compressive applied load, first (ε_{p1}) and third (ε_{p3}) principal strains and maximum shear strain (γ_{max}) were computed within the bone-biomaterial volume after a bi-cubic interpolation of the measured strain to allow a strain value per voxel. Histograms of the strain distribution were calculated as the number of voxels for bone/biomaterial with strains corresponding to a specific bin, divided by the total number of mineralised voxels. 1000 bins were used to cover a range from 0 με to ±10000 με for the first and third principal strains, and 0 με to 15000 με for the shear strain. Additionally, the yielded solid volume (SV_y) was computed as the mineralised voxels exceeding +/-10000 με in tension/compression, or above 15000 με in shear [68,69].

2.6. Multi-scale microCT

Following the *in situ* mechanical test, multi-scale microCT was performed in the bone-biomaterial systems to acquire high-resolution images in regions of newly formed bone. MicroCT was performed (ZEISS Xradia Versa 510) at three different resolutions (4 μm, 1.5 μm and 0.5 μm voxel size) using the 'scout-and-zoom' workflow available in the system and different optical magnification. Firstly, medium-resolution (4 μm voxels) was set using 60 kV at 0.4X optical magnification with an exposure time of 5 seconds per projection in order to have the entire specimen diameter in the field of view (~ 4 mm). Then, a VOI (1.5 mm^3) at the bone-biomaterial interface was identified and a high-resolution (1.5 μm voxels) acquisition was performed using 60kV energy at 4X optical magnification with an exposure time of 6 seconds. Finally, the 'zoom-in' process converged on a smaller VOI (0.5 mm^3) from the second

reconstructed volume to include some remaining bone graft material and most of the newly formed bone. The highest-resolution (0.5 µm voxels) imaging was conducted at 80kV and a 20X optical magnification with an exposure time of 30 seconds per projection. 2001 projections were acquired for the three tomograms at a rotational step of 0.18°, resulting in a total scanning time of 23 hours per specimen approximately.

3. RESULTS

3.1. *In situ* SR-microCT mechanics

The extracted bone-biomaterial specimens presented a large variation in their SV (Table 1), ranging from 38% for the bone-ApaPore to 48% for bone-Actifuse, which also presented the highest GV/TV. In all bone-biomaterial systems the BV/TV was higher than in the trabecular bone specimen. The orientation and positioning of the graft boundary also differs among the specimens (Figure 2). Whereas bone-ApaPore presented an almost continuous path of graft material from bottom to top in an almost vertical orientation, bone-Actifuse, bone-StronBone and bone-StronBone-P showed the remaining graft localised mostly at one of the ends of the specimen at various angles.

Table 1. Solid volume fraction (SV/TV) in the four bone-biomaterial and the control specimens computed from the reconstructed SR-microCT images prior to loading. A quantification of the bone volume fraction (BV/TV) and graft volume fraction (GV/TV) is also shown for the bone-Actifuse, bone-ApaPore and bone-StronBone-P systems. Bone-StronBone specimen did not provide enough contrast to segment the graft material from the bone tissue.

	SV/TV (%)	BV/TV (%)	GV/TV (%)
Actifuse	48.0	38.5	9.5
ApaPore	38.0	25.6	12.5
StronBone	41.8	---	---
StronBone-P	40.7	34.8	5.9
Control	---	23.6	---

The force-displacement curves (Figure 3) showed an initial toe region, followed by a monotonic trend that was linear during the first two steps up to 0.25 mm of compression. Stress relaxation was also visible at the end of each compression step, when the actuator was stopped to allow SR-microCT scanning. Failure was considered at the point where force reached a plateau or eventually dropped. This occurred either during the third step (bone-StronBone), or during the fourth step (all others). The bone-StronBone specimen presented a more ductile behaviour with respect to the others, and failure was only reached after 1 mm of compression. On the other hand, the bone-Actifuse seemed to be much stiffer, and failure was reached for an applied load an order of magnitude higher than the other specimens (160 N for bone-Actifuse compared to ~60N for bone-ApaPore). Bone-ApaPore and bone-StronBone-P specimens showed behaviour more similar to the trabecular bone control, with elastic regions fairly parallel. Furthermore, failure for bone-StronBone-P and control specimens was experienced at a similar point (~ 50 N force and ~ 0.8 mm compression).

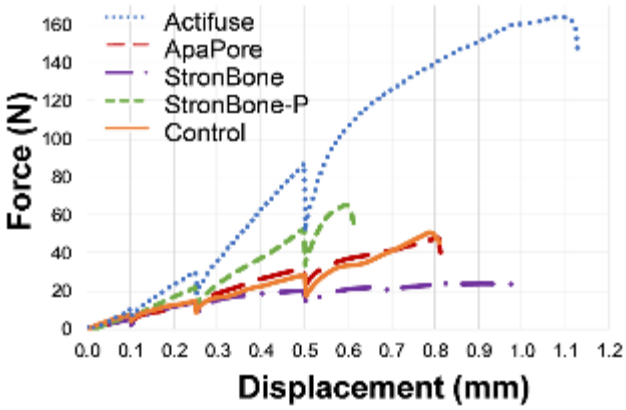

Figure 3. Load-displacement curves for the tested specimens. The force shows a drop at the end of each compression step, corresponding to the stress relaxation while the specimen was allowed to settle (10 min) before image acquisition (~2 min).

A qualitative inspection of the SR-microCT images of the four bone-biomaterial systems before and after failure (Figure 4) showed the different integration of the bone graft materials within the bone matrix. SR-microCT evaluation clearly distinguished the three distinct materials that were present: bone marrow (dark grey), bone tissue gradients (medium greys), and remaining bone graft (light grey). In addition, the newly formed bone was easily recognisable in proximity of the remaining biomaterial and differs from the more remodeled trabecular bone, present in bone-ApaPore and bone-Actifuse specimens, in the more amorphous organisation (i.e. woven type). A comparison of the SR-microCT images before and after failure revealed how microdamage accumulated during *in situ* compression mainly developed in proximity (Actifuse- ApaPore-bone) or within (StronBone- StronBone-P-bone) the new regenerated tissue. Failure in bone-Actifuse and bone-ApaPore specimens degenerated in trabecular fracture, whereas microcracks were clearly visible in the newly formed bone at the bone-biomaterial interface for the bone-StronBone-P. Microdamage in bone-StronBone was not detected by visual inspection, in accordance to the fact that overall failure was not identified (Figure 3).

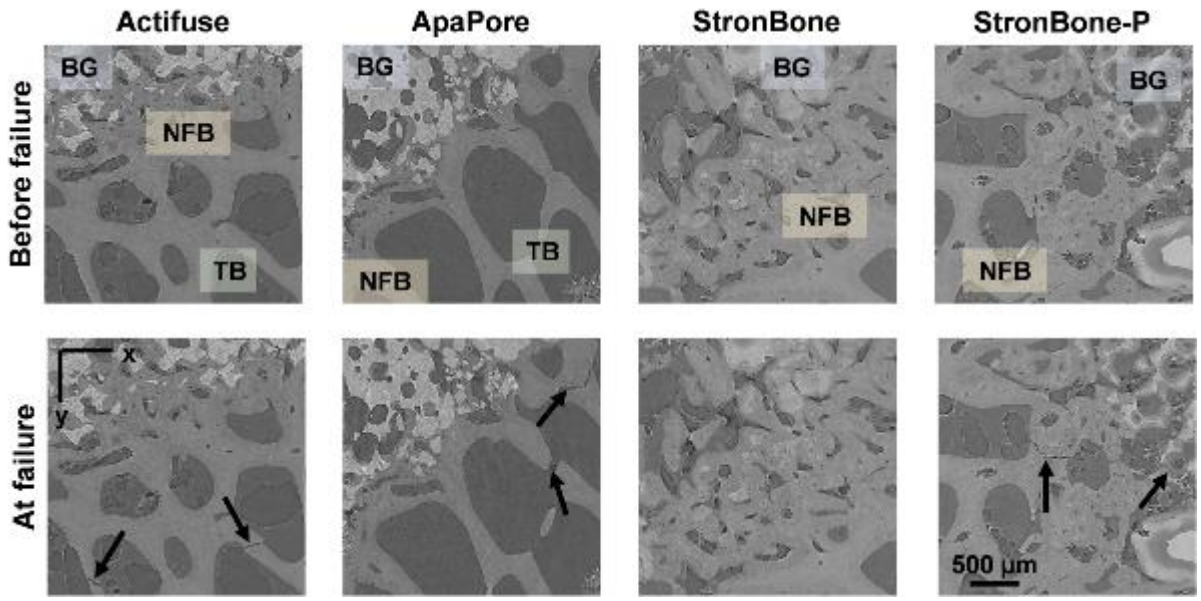

Figure 4. SR-microCT cross-sections through the VOI of each bone-biomaterial system before (top) and after (bottom) failure. Areas corresponding to trabecular bone (TB), newly formed bone (NFB) and bone graft material (BG) are indicated in the top row before failure. Arrows in the bottom row of images indicate visible microcracks developed either in the pre-existing bone for bone-Actifuse and bone-ApaPore or in the newly formed bone for bone-StronBone and bone-StronBone-P after mechanical loading. Samples were compressed in the z direction, perpendicular to the shown cross-sections. Scale bar is valid for all images.

3.2. Digital volume correlation

The third principal strain distributions (ε_{p3}) for the four compression steps are reported in Figure 5 for a representative VOI (1.6 x 1.6 x 1.0 mm^3) including the bone-biomaterial interface. A strain accumulation in regions of trabecular bone was observed for the bone-Actifuse and bone-ApaPore specimens (Figure 5, first and second row), where failure was located at the end of the test. After the second compression step (Δl = 0.25 mm) a strain redistribution appeared in bone-Actifuse specimen; however, a further increase in the applied load (third step, Δl = 0.5 mm) led to higher compressive strains in the original (Δl = 0.1 mm) more strained areas, which further developed in trabecular fracture. Additionally, after fracture,

the structure lacked support for load transfer; thus, high differences of residual strain were observed between the fractured regions (trabecular bone) and the undamaged ones (bone graft). The compressive strain distribution of bone-StronBone and bone-StronBone-P presented an opposite behaviour due to the differences of graft integration within the newly formed bone (Figure 4). Bone-StronBone system (Figure 5, third row) showed strain accumulation mainly in areas of newly formed bone, whereas areas in which bone graft remained unabsorbed presented low strain levels. Conversely, higher compressive strains were found in the bone graft regions for the bone-StronBone-P system (Figure 5, fourth row) and low strain values in the newly formed tissue.

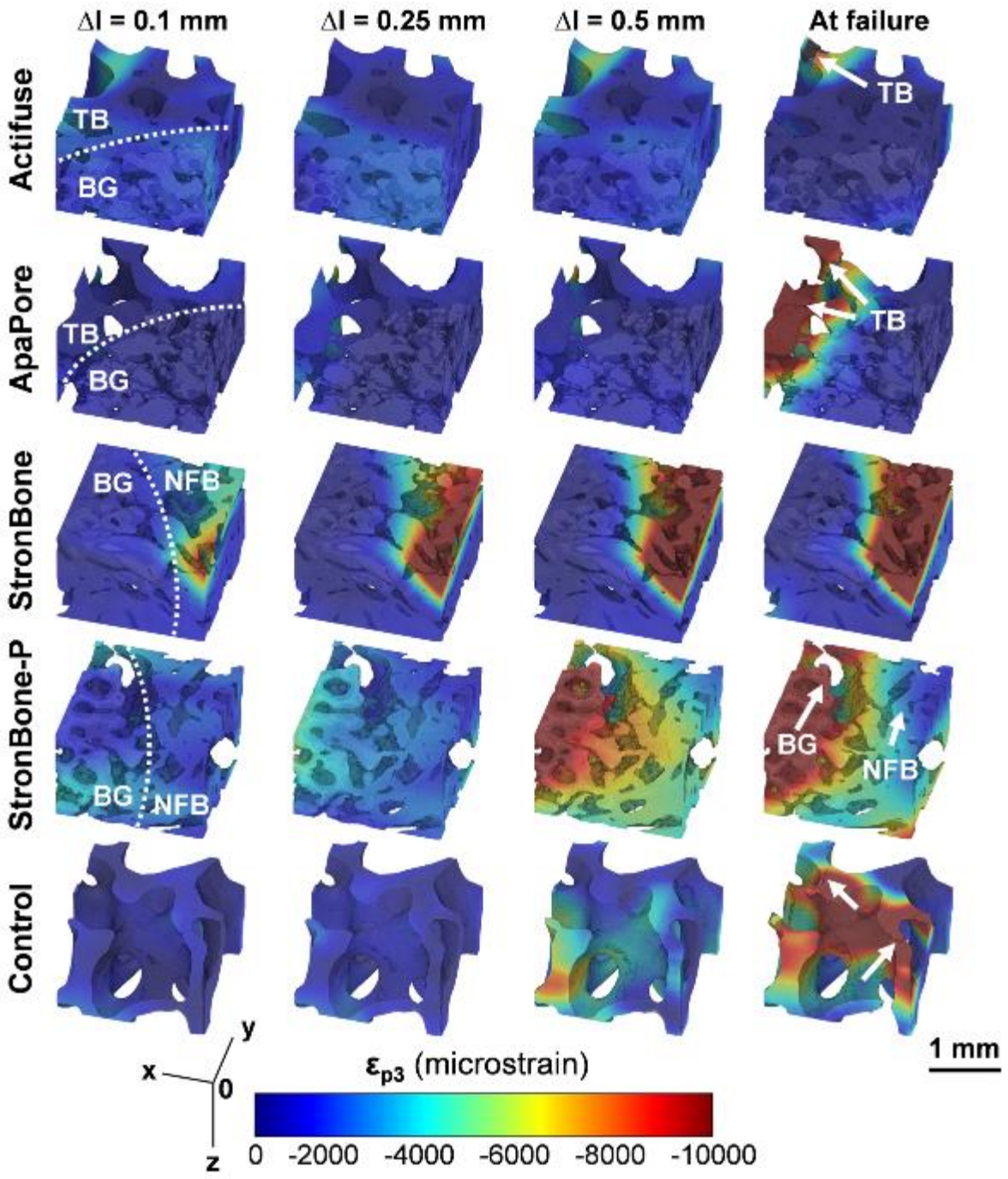

Figure 5. 3D full-field third principal strain distribution (ε_{p3}) at each compression step for the bone-biomaterial systems and the trabecular bone control. A representative VOI (1.6 x 1.6 x 1.0 mm^3) at the bone-biomaterial interface was analysed. Bone-biomaterial interface is indicated by a dotted line in the first column. Microcracks after failure are indicated with arrows as well as material in which failure was observed. Samples were compressed in the z direction. TB: Trabecular bone; NFB: newly formed bone; BG: bone graft material.

Full-field first principal strain (ε_{p1}) and shear strain (γ_{max}) distributions are reported in Figure 6 and 7, respectively, for all the specimens. A similar strain behaviour for the compressive strain (ε_{p3}) was observed for the bone-Actifuse and bone-ApaPore specimens, in which the strain development seemed to predict the failure in the trabecular bone regions. Tensile strains in bone-StronBone (Figure 6, third row) were considerably lower than compressive strains, whereas an important difference in the shear and compressive strain between areas of remaining bone graft and newly formed bone was observed (Figure 7, third row) in the same specimen. On the other hand, the distribution of tensile and shear strains in the bone-StronBone-P (Figures 6 and 7, fourth row) at failure differed from the compressive strains, as higher strain magnitudes were identified along the microcracks developed through the bone-biomaterial interface.

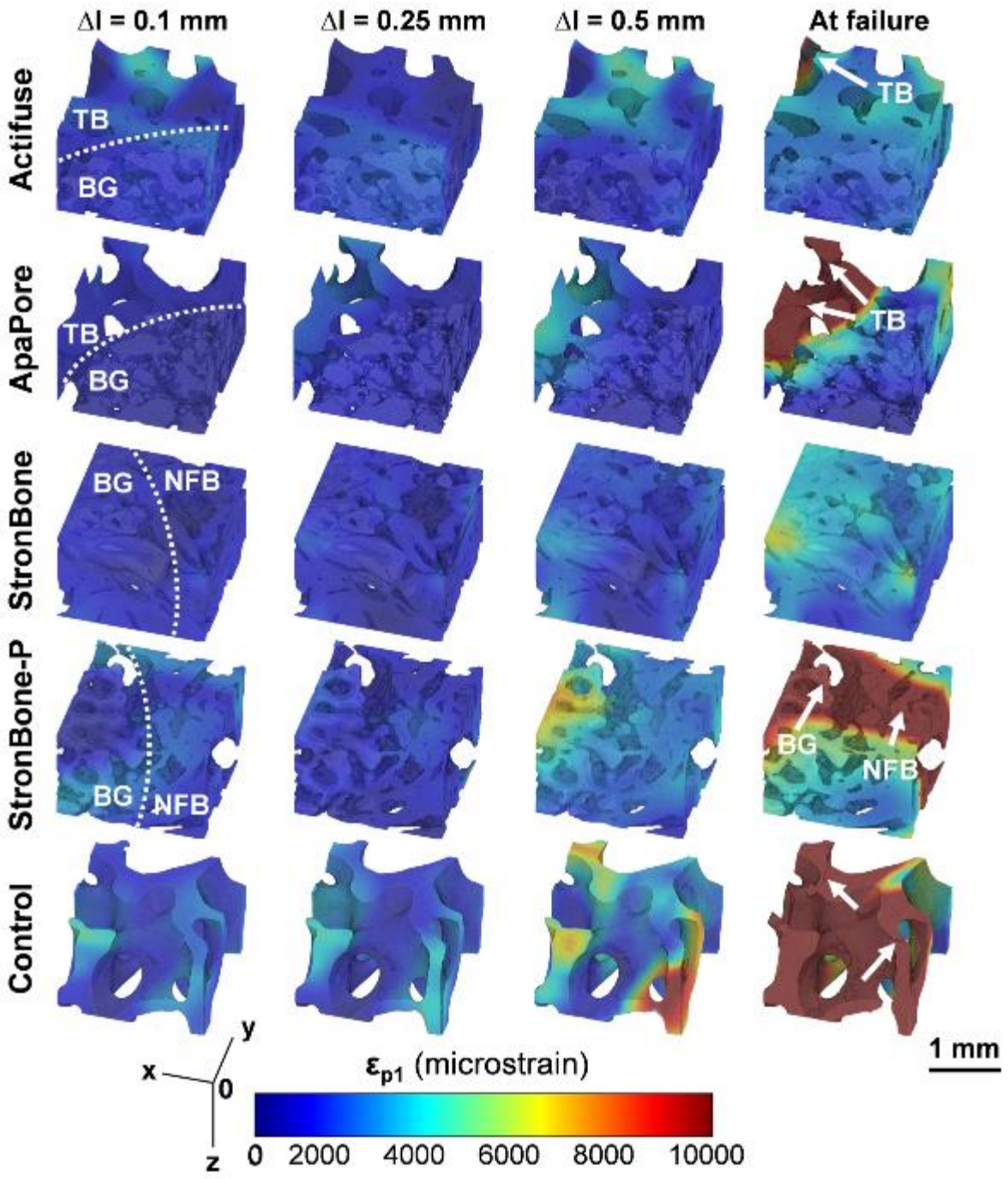

Figure 6. 3D full-field first principal strain distribution (ε_{p1}) at each compression step for the bone-biomaterial systems and the trabecular bone control. A representative VOI (1.6 x 1.6 x 1.0 mm^3) at the bone-biomaterial interface was analysed. Bone-biomaterial interface is indicated by a dotted line in the first column. Microcracks after failure are indicated with arrows as well as material in which failure was observed. Samples were compressed in the z direction. TB: Trabecular bone; NFB: newly formed bone; BG: bone graft material.

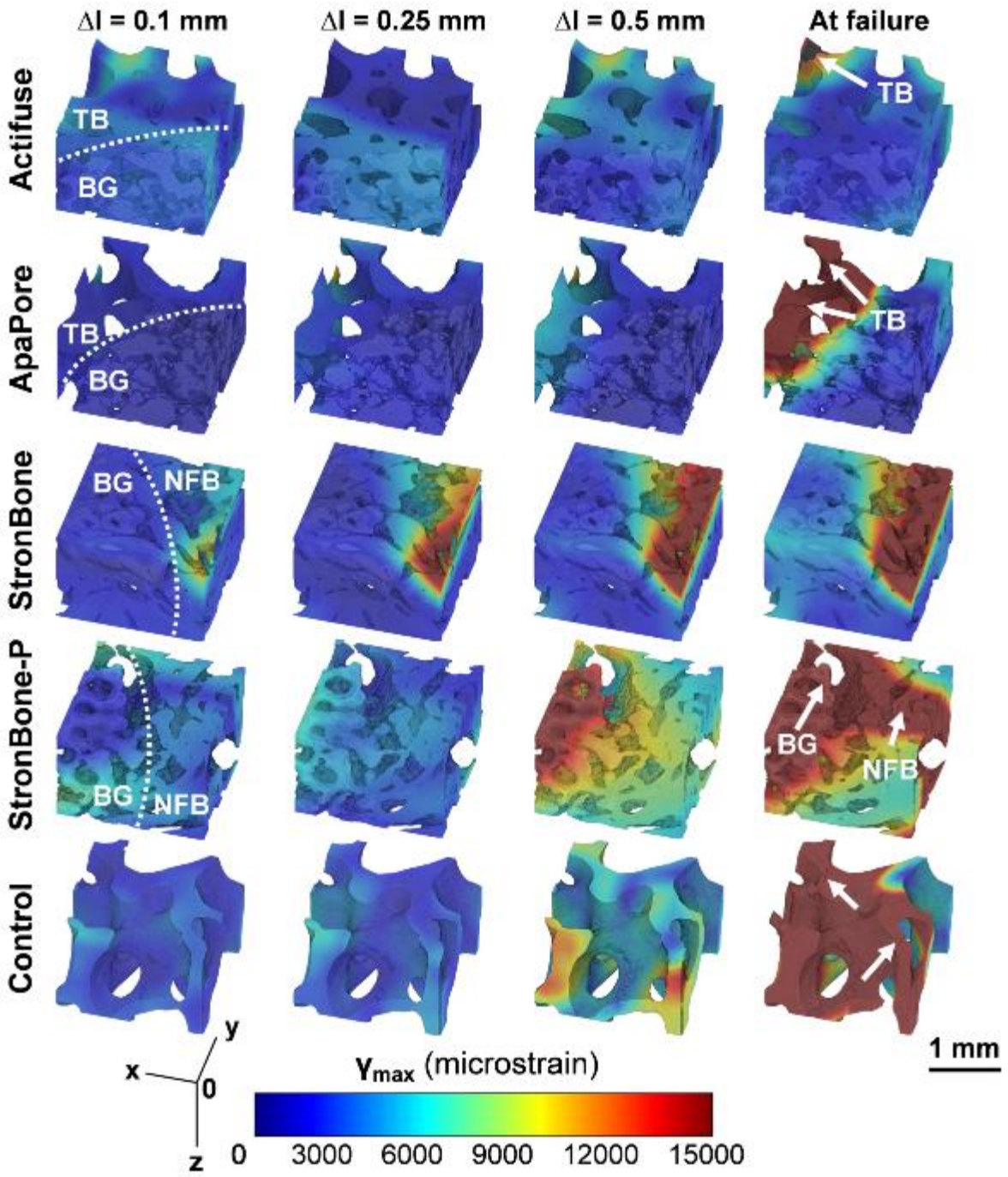

Figure 7. 3D full-field maximum shear strain distribution (γ_{max}) at each compression step for the bone-biomaterial systems and the trabecular bone control. A representative VOI (1.6 x 1.6 x 1.0 mm^3) at the bone-biomaterial interface was analysed. Bone-biomaterial interface is indicated by a dotted line in the first column. Microcracks after failure are indicated with arrows as well as material in which failure was observed. Samples were compressed in the z direction. TB: Trabecular bone; NFB: newly formed bone; BG: bone graft material.

The yielded solid volume (Table 2) after failure emphasised the different behaviour for the bone-Actifuse and bone-ApaPore compared to bone-StronBone and bone-StronBone-P specimens. The first two presented a small percentage of damaged volume, which was more important in the bone tissue than in the remaining bone graft, and a higher yielded volume was reached in a combination of tensile and shear states. On the contrary, a yielded solid fraction started to accumulate in the bone-StronBone right after the first compression step, resulting in over 25% of damaged volume after the third step and 40% after failure in both compression and shear. The yielded volume after failure for the bone-StronBone-P was also over 40% in tensile and shear and it was more important in the biomaterial region than in the bone tissue area. Tensile and shear strains seemed also more damaging in the trabecular bone control specimen, with 30% of its volume yielded after failure.

Table 2. Yielded solid volume in tension ($SV_{y, \varepsilon p1}$), compression ($SV_{y, \varepsilon p3}$) and shear ($SV_{y, \gamma max}$) after failure in the four bone-biomaterial and the control specimens, as computed using DVC. SV_y was computed as the hard phase voxels exceeding +/- 10000 με in tension/compression, or above 15000 με in shear.

		$SV_{y\ \varepsilon p1}$ (%)	$SV_{y, \varepsilon p3}$ (%)	$SV_{y, \gamma max}$ (%)
Actifuse				
	Bone	0.79	0.23	0.83
	Biomaterial	0	0	0
ApaPore				
	Bone	10.89	5.37	8.99
	Biomaterial	0.02	0.02	0.02
StronBone				
	Bone	25.63	42.43	42.49
	Biomaterial	---	---	---
StronBone-P				
	Bone	45.53	17.43	43.99
	Biomaterial	50.21	38.08	57.03
Control				
	Bone	30.54	13.52	29.85
	Biomaterial	---	---	---

The histograms of shear strain (Figure 8) for the first and last compression steps well described the strain evolution in the bone and biomaterial areas of the analysed specimens. As expected, maximum amplitudes were reached for lower strain values after the first compression step compared to the last (failure). Additionally, peak values corresponded to lower strains in the biomaterial areas in bone-Actifuse and bone-ApaPore, but to higher strain levels in the StronBone-P.

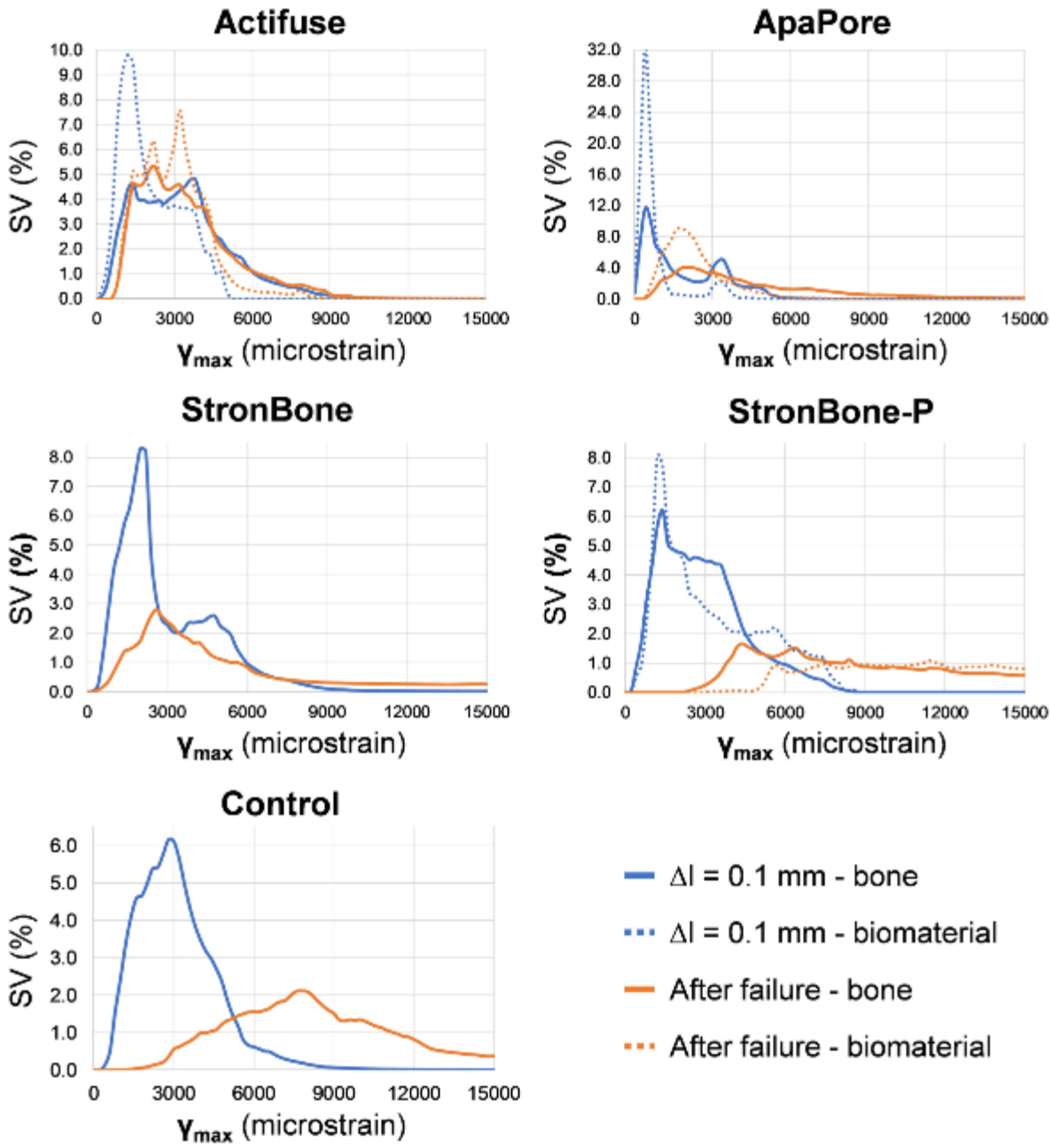

Figure 8. Histograms of the maximum shear strain distribution (γ_{max}) in the hard phase (bone-biomaterial) of the VOI as computed using DVC for the first compression step (blue) and after failure (orange). Values exceeding 15000 με are reported in Table 2. A partition of the strain in the bone (trabecular and newly formed, solid line) and biomaterial (bone graft, dotted line) is shown for the bone-Actifuse, bone-ApaPore and bone-StronBone-P specimens. Bone-StronBone specimen did not show enough contrast (Figure 4) to segment the graft material from the bone tissue.

3.3. Multi-scale microCT

High resolution microCT images (Figure 9) provided morphological and degree of mineralisation information that allowed for differentiation of trabecular bone, newly formed bone and remaining bone graft, as well as the osteoconduction around the graft material. Bone-Actifuse and bone-ApaPore showed minimal dissolution of the biomaterial, with large areas of remnants with no signs of resorption. Bone formation was identified within the graft granules and in their proximity. More newly formed bone tissue, characterised for highly disorganised structure compared to the native trabecular structure, was observed in the bone-Actifuse. However, bone-ApaPore presented a more organised bone formation directly from the graft material. Bone-StronBone and bone-StronBone-P specimens also showed some remnants of biomaterial in the bone defect areas; however, resorption was observed within the newly formed bone regions, characterised for a higher mineral density (lighter grey-level). The interface between the biomaterial and bone was almost completely assimilated (Figure 9-I) but some gaps were visible at higher magnification (Figure 9-II, III, green arrows) in bone-Actifuse, bone-ApaPore and bone-StronBone-P. For all bone-biomaterial systems bone was identified not only in contact with the outer surface of the graft but also within its pores (Figure 9, blue arrows). The higher-resolution scans enabled identification of osteocyte lacunae within the newly formed bone (Figure 9-III, yellow arrows). Furthermore, the larger pores found in the newly formed bone may correspond to blood vessel formation (Figure 9-III, white arrows). Additionally, cracks in the ApaPore and StronBone-P, most likely associated with the bone impaction grafting procedure, could be identified at the highest resolution (Figure 9-II, III, red arrows).

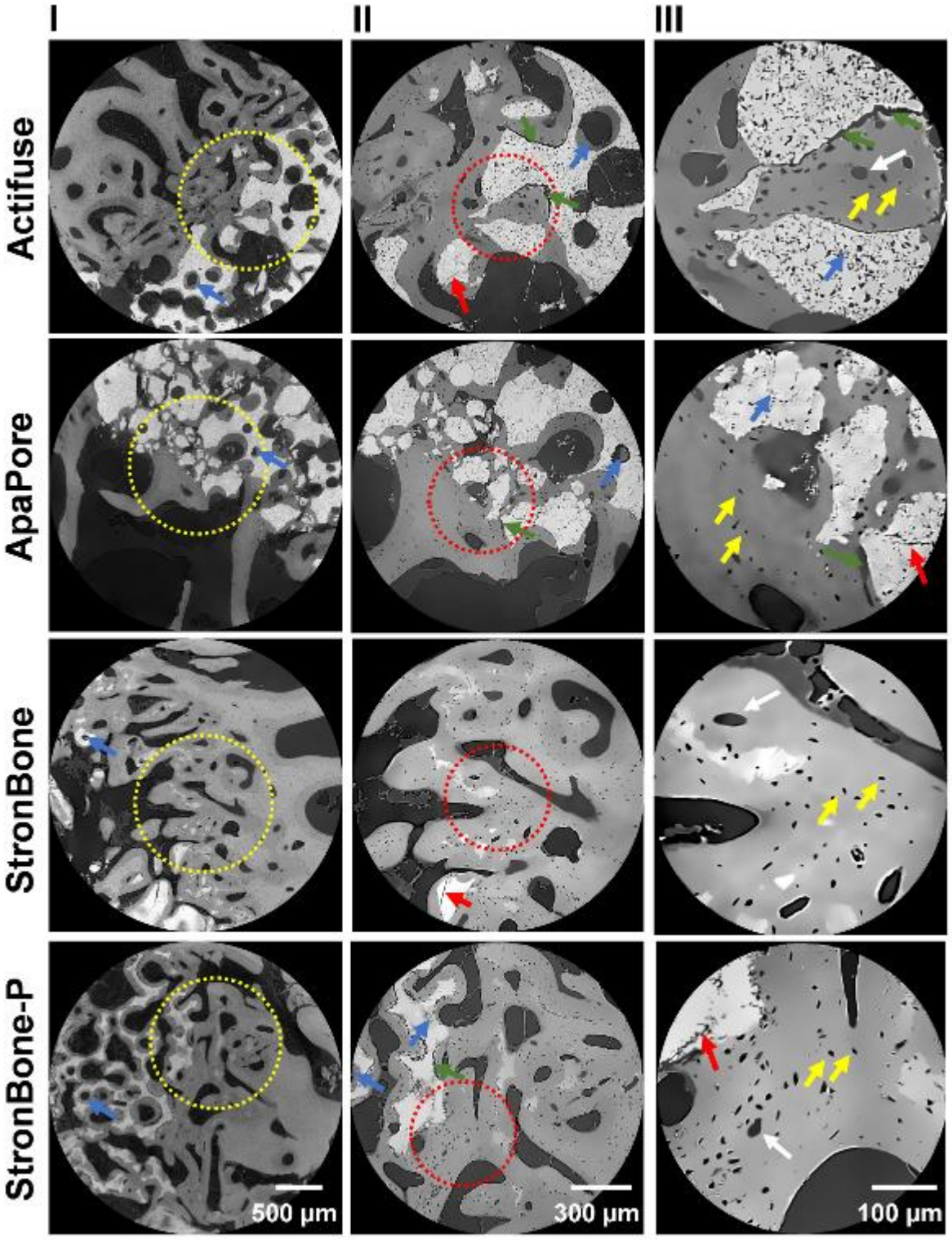

Figure 9. Multi-scale microCT images of the bone-biomaterial systems obtained by increasing the spatial resolution. Images were first acquired at a medium resolution (4 μm^3 voxel size, I). A VOI (yellow circle) was selected and a higher resolution acquisition was performed (1.5 μm^3 voxel size, II). A second VOI (red circle) was then chosen to achieve the highest resolution

(0.5 µm^3 voxel size, III). Bone formation was observed within pores (blue arrows), and some gaps were visible at the bone-biomaterial interface (green arrows). Bone graft material presented some cracks (red arrows). Osteocyte lacunae (yellow arrows), and blood vessels (white arrows) were identified at the highest resolution. Scale bars are valid for all images in the same column.

4. DISCUSSION

The aim of this study was to investigate and quantify the full-field strain distribution of bone-biomaterial systems produced *in vivo* by osteoregenerative bone graft materials, combining *in situ* SR-microCT mechanical testing and DVC. More specifically, this work aimed at evaluating the internal strain and microdamage progression of such composites, and the specific strain distribution in bone graft remnants, newly formed bone and trabecular bone. Despite the fact that synthetic bone grafts have shown excellent performance in terms of bone regeneration [17], their mechanical competence is partially unexplored [47,48].

At an apparent level similar forces were observed within the elastic range for the bone-biomaterial systems and the control trabecular bone sample, which then differed with load progression (Figure 3). However, a comparison of the apparent behaviour of the studied composites is challenging, as it depends not only on the distinct implanted bone graft material, but also on their integration during the regeneration process and their volume fraction. Variation in the sample extraction prevented fine control of the graft volume and orientation within the individual specimens (Figure 2), which ultimately affected the apparent mechanics. Bone-Actifuse showed the stiffest behaviour (Figure 3), which may be related to the higher solid volume fraction (Table 1) compared to the other systems. It is interesting to note differences in the apparent mechanics of bone-bioglass systems, where bone-StronBone presented a highly ductile behaviour and bone-StronBone-P was much stiffer (Figure 3). Both systems had a similar solid volume fraction (Table 1) and graft location (Figure. 2), but the

variations in the biomaterial integration (Figure 9) play an important role in their dissimilarities. The higher resorption and integration of StronBone compared to StronBone-P lead to denser regions of newly formed bone (Figure 9) with different mineralisation levels in bone-StronBone, which may affect the viscoelasticity of the specimen. It is also worth noticing the similar apparent behaviour of bone-ApaPore system and the trabecular bone control specimen, regardless of their different solid volume fraction, composition and morphometry. A better and more accurate characterisation of the mechanical properties of newly bone formed could be achieved using different mechanical tests (i.e. micro-, nanoindentation), in which the variations of the biomaterial within each sample would not limit interpretation of the results. Particularly, Gauthier at al., [41] measured the compressive strength of the newly regenerated tissue after implantation of an injectable bone substitute using microindentation, showing that the implanted biomaterial could support the formation of new bone with compressive strength higher than in the native trabecular tissue. Similar findings have been shown in bone-StronBone (Figure 5, third row), in which damage was not visible regardless of the high levels of compressive strain identified.

The results herein reported showed that the main microfailure events seemed to be localised close to, or within, the newly formed bone (Figure 4) at the bone-biomaterial interface. The higher stiffness and strength of the bone graft compared to the more remodelled trabecular tissue induced a critical region at the boundary of the bone-biomaterial, where the initiation of the failure was identified, consistent with previous reports on bone-cements composites [43,47,48]. Furthermore, the high-resolution SR-microCT images used in this study allowed for the detection of microdamage (i.e. microcracks) in the tissue (Figure 4); thus, providing a deeper insight of the deformation mechanisms at the bone-biomaterial interface. Danesi el al. [48] and Tozzi et al. [43,47] characterised the damage progression in bone-cement composites using microCT images obtained in a lab-based system at 39 µm and 20 µm, respectively. However,

the image spatial resolution was not enough to characterise the deformation at a tissue scale. In fact, this is the first time that a characterisation of the microdamage evolution of bone-biomaterial composites at the tissue level has been performed, allowing not only the visual identification of the internal microdamage at the boundary of bone and biomaterial, but also the quantification of the localised strain in both materials. The potential of DVC based on SR-microCT images to characterise bone deformation at the tissue level remains partially unexplored [51,62] and questions still arise on the effect of high-flux SR X-ray radiation on the mechanical properties of the tissue [70]. However, this study limited the total radiation dose absorbed by the tissue (~30 kGy) following previous methodologies [62] in order to minimise the effect of the X-ray radiation on the mechanical integrity of the specimens.

DVC successfully showed how local strains built up from the elastic regime highlighting internal weaker areas that could further result in microdamage initiation and progression to failure (Figures 5, 6, 7). A complex load transfer was developed in the highly heterogeneous composite structures during compression and the DVC-computed 3D full-field strain allowed for a description of the microdamage progression. Particularly, high levels of compressive strain, above the typical values of trabecular bone yielding [71,72], were found in areas of trabecular bone fracture (Figure 5) in bone-Actifuse, bone-ApaPore and control specimens. Interestingly, localised strain concentration was observed in bone-Actifuse system (Figure 5, top row) from the first compressive step, resulting in fractured regions at the final compression step. Although bone-StronBone presented high compressive strains since early stages of compression in areas of newly formed bone (Figure 5, third row), microdamage was not visible. This highlighted the important ability of bone to accumulate microdamage at the tissue level prior to the initiation of microcracks [51,73]. The localisation of highly strained regions during the initial steps of compression in bone-Actifuse, bone-StronBone (Figure 5) and bone-StronBone-P (Figure 7) demonstrated how yielding probably started at low stress levels, as previously

reported at the nanoscale in bone tissue [74,75]. Even though the specimens were subjected to compressive loading, initiation and propagation of microcracks in bone-StronBone-P system were not related to compressive strains but shear strains (Figure 7, fourth row). Christen et al. [51] showed similar findings during microcrack propagation in cortical bone. While compressive (Figure 5) and tensile (Figure 6) strain magnitudes were comparable, a higher tensile strain accumulation was found around microcracks and trabecular bone fractured regions. As suggested by Christen et al. [51], tensile strains could be used to detect microcracks in the first place. In fact, the tensile strain evolution in bone-Actifuse, bone-ApaPore, bone-StronBone-P and control specimens (Figure 6) seemed to predict the initiation of internal microdamage before it was visible.

The strain partition between bone and biomaterial in bone-Actifuse, bone-ApaPore and bone-StronBone-P systems indicated how the different resorption mechanism of the distinct graft materials affected the load transfer and therefore, the microdamage progression. In particular, the slower resorption of Actifuse and ApaPore (Figure 4), with higher stiffness of the biomaterial compared to the bone tissue, induced an insufficient load transfer from the trabecular bone tissue towards the bone graft regions. Therefore, producing higher strains in bone areas (Figure 8) that ultimately induced microdamage in the trabeculae (Table 2). Conversely, the faster resorption of StronBone-P and better integration within the newly formed bone (Figure 4) produced a more effective load transfer throughout the specimen, leading to a more equal strain distribution (Figure 8) and microdamage at the interface (Figure 4). Similar findings were reported by Tozzi el al. [47] and Goodheart et al. [76] for bone-cement composites. It was shown that the accumulated strain in the biomaterial region and the bone-cement interface was much lower compared to the trabecular bone when the two phases were clearly distinct, but a better load transfer through the interface was found in the more integrated composites. Recently, Li et al. [36] suggested that the presence of grafts remnants in the defect

area may provide adequate mechanical support during healing. However, the results herein presented showed that when the biomaterial is less resorbed (bone-Actifuse and bone-ApaPore) load cannot be transferred in an efficient way, leading to a highly heterogenous strain distribution with large localised peaks in the pre-existing bone tissue that may cause bone fracture in the event of an overload postoperatively. Conversely, the more immature tissue filling the defect after faster degradation of StronBone and StronBone-P was able to carry the load in a more satisfactory way and the structure did not collapse at the end of the compression test. Additionally, microdamage was not observed in bone-StronBone system suggesting that, although the newly formed bone was still very immature and partially remodelled, it was able to fulfil and exceed the mechanical performance of the native tissue. These results indicate that a faster resorption rate and higher osteoinduction of synthetic bone grafts for bone replacement may be beneficial for efficient micromechanics *in vivo* in a postoperative overloading scenario. The multi-scale microCT results provided a 3D characterisation of bone regeneration induced by the action of osteoconductive biomaterials. The analysis of *in vivo* biomaterial-induced bone repair has traditionally been assessed using scanning electron microscopy (SEM) combined with histological analysis [35,36,39,40,77,78]. The traditional methods produce valuable data on bone-biomaterial interactions relating the morphology, amount and functional properties of the newly formed bone, however they are restricted to sample sectioning and only surface analysis can be conducted. Therefore, microCT shows a clear advantage to describe bone-biomaterial interfaces *ex vivo*. Similar to previous SEM analysis [77,79], bone ingrowth was observed within biomaterials (Figure 9, blue arrows). When compared to published histological analysis [36,78], osteocyte lacunae (Figure 9-III, yellow arrows) were found in the new bone and gaps between the bone and biomaterial (Figure 9-II, III, green arrows), suggesting the presence of loose connective tissue. This multi-scale microCT approach could be combined with *in situ* mechanics and DVC to obtain not only the 3D characterisation of bone-biomaterial composites,

but also to provide the deformation mechanisms at different scales, from apparent to tissue level. Through the correlation of DVC-measured strains at multiple resolutions to complementary data such as histology or local material properties, a deeper understanding of the *in vivo* bone repair through the action of biomaterials could be achieved.

The results of this study revealed important details of the bone-biomaterial interactions and micromechanics in a clinically relevant bone defect model using synthetic bone graft substitutes. The strain analysis of bone-biomaterial composites after *in vivo* service in the ovine model was performed for the first time; thus, providing clinical relevant biomaterial-tissue integration compared to previous experiments carried out *in vitro* [43,47,48]. The current study is limited considering that only one time point (6 weeks after implantation) was evaluated. However, the outcomes herein presented can be considered as a representative case for the event of an overload during *in vivo* service in a postoperative period. The inability of bone graft materials to restore bone mechanical functions could jeopardise the surgical intervention, with consequent clinical and economic impact. Furthermore, due to the limited sample size (one specimen per group) and the dissimilarities among those, the generalisation of the results will need further analysis. These findings have the potential to inform numerical models of bone tissue and bioresorbable material adaptation, enabling predictions of the long-term *in vivo* behaviour of such grafts in the repair of critical size bone defects. Such models could be used for a deeper study of bone-biomaterial micromechanics, in which more physiological relevant loading and boundary conditions are considered. Additional insights may be also gained by increasing the sample size, comparing the bone repair processes and full-field strain at the bone-biomaterial interface among different bone graft substitutes at different implantation times.

5. CONCLUSION

The combination of high-resolution SR-microCT images and DVC has allowed characterisation, for the first time, of the full-field strain in bone-biomaterial systems produced *in vivo* in an ovine critical size bone defect model. It has been shown that complex strain patterns developed through the highly heterogeneous composites during compression are promoting primary microdamage, either in the pre-existing trabecular bone or in the newly formed bone, at the bone-biomaterial interface. DVC allowed for a detailed analysis of the internal strain distribution and its association with the microdamage initiation and progression in proximity to the bone-biomaterial interface. These findings highlight the importance of understanding the interaction and micromechanics of bone graft materials and bone tissue. The outcomes of this study have the potential to facilitate biomaterial development and predictions of long-term bone healing following biomaterial implantation.

ACKNOWLEDGMENTS

The authors gratefully acknowledge Diamond Light Source for beamtime at the Diamond-Manchester Imaging Branchline I13-2 and its associated Data Beamline [80] (proposal number MT14080), and the Zeiss Global Centre (University of Portsmouth) for image processing. We further acknowledge Dr Dave Hollis (LaVision Ltd) for assistance with DaVis software, Dr Kazimir Wanelik for help during the experiment at Diamond Light Source, Dr Alexander Kao for support during multi-scale microCT imaging and proof-reading the manuscript, and Dr Robin Rumney for the fruitful discussions.

REFERENCES

(1) Sims, N. A.; Gooi, J. H. Bone Remodeling: Multiple Cellular Interactions Required for Coupling of Bone Formation and Resorption. *Semin. Cell Dev. Biol.* **2008**, *19* (5), 444–451. https://doi.org/10.1016/j.semcdb.2008.07.016.

(2) Oryan, A.; Monazzah, S.; Bigham-Sadegh, A. Bone Injury and Fracture Healing

Biology. *Biomed. Environ. Sci.* **2015**, *28* (1), 57–71. https://doi.org/10.3967/bes2015.006.

(3) Schubert, T.; Lafont, S.; Beaurin, G.; Grisay, G.; Behets, C.; Gianello, P.; Dufrane, D. Critical Size Bone Defect Reconstruction by an Autologous 3D Osteogenic-like Tissue Derived from Differentiated Adipose MSCs. *Biomaterials* **2013**, *34* (18), 4428–4438. https://doi.org/10.1016/j.biomaterials.2013.02.053.

(4) Giannoudis, P. V.; Einhorn, T. A.; Marsh, D. Fracture Healing: The Diamond Concept. *Injury* **2007**, *38* (4 SUPPL.), 3–6. https://doi.org/10.1016/S0020-1383(08)70003-2.

(5) Faour, O.; Dimitriou, R.; Cousins, C. A.; Giannoudis, P. V. The Use of Bone Graft Substitutes in Large Cancellous Voids: Any Specific Needs? *Injury* **2011**, *42* (SUPPL. 2), S87–S90. https://doi.org/10.1016/j.injury.2011.06.020.

(6) Campana, V.; Milano, G.; Pagano, E.; Barba, M.; Cicione, C.; Salonna, G.; Lattanzi, W.; Logroscino, G. Bone Substitutes in Orthopaedic Surgery: From Basic Science to Clinical Practice. *J. Mater. Sci. Mater. Med.* **2014**, *25* (10), 2445–2461. https://doi.org/10.1007/s10856-014-5240-2.

(7) Schroeder, J. E.; Mosheiff, R. Tissue Engineering Approaches for Bone Repair: Concepts and Evidence. *Injury* **2011**, *42* (6), 609–613. https://doi.org/10.1016/j.injury.2011.03.029.

(8) Bloemers, F. W.; Blokhuis, T. J.; Patka, P.; Bakker, F. C.; Wippermann, B. W.; Haarman, H. J. T. M. Autologous Bone versus Calcium-Phosphate Ceramics in Treatment of Experimental Bone Defects. *J. Biomed. Mater. Res. B. Appl. Biomater.* **2003**, *66* (2), 526–531. https://doi.org/10.1002/jbm.b.10045.

(9) Sen, M. K.; Miclau, T. Autologous Iliac Crest Bone Graft: Should It Still Be the Gold Standard for Treating Nonunions? *Injury* **2007**, *38* (SUPPL. 1), 2–7. https://doi.org/10.1016/j.injury.2007.02.012.

(10) Dimitriou, R.; Mataliotakis, G. I.; Angoules, A. G.; Kanakaris, N. K.; Giannoudis, P. V. Complications Following Autologous Bone Graft Harvesting from the Iliac Crest and Using the RIA: A Systematic Review. *Injury* **2011**, *42* (SUPPL. 2), S3–S15. https://doi.org/10.1016/j.injury.2011.06.015.

(11) Banwart, J. C.; Asher, M. A.; Hassanein, R. S. Iliac Crest Bone Graft Harvest Donor Site Morbidity: A Statistical Evaluation. *Spine (Phila. Pa. 1976).* **1995**, *20* (9).

(12) Wheeler, D. L.; Enneking, W. F. Allograft Bone Decreases in Strength in Vivo over Time. *Clin. Orthop. Relat. Res.* **2005**, No. 435, 36–42.

(13) Mankin, H. J.; Hornicek, F. J.; Raskin, K. A. Infection in Massive Bone Allografts.

Clin. Orthop. Relat. Res. **2005**, *432*.

(14) Fillingham, Y.; Jacobs, J. Bone Grafts and Their Substitutess. *Bone Jt. J.* **2016**, *98–B* (1 Suppl A), 6–9. https://doi.org/10.1302/0301-620X.98B1.36350.

(15) Roberts, T. T.; Rosenbaum, A. J. Bone Grafts , Bone Substitutes and Orthobiologics Bone Grafts , Bone Substitutes and Orthobiologics The Bridge between Basic Science and Clinical Advancements in Fracture Healing. **2016**, *6278* (February), 114–124. https://doi.org/10.4161/org.23306.

(16) Giannoudis, P. V.; Dinopoulos, H.; Tsiridis, E. Bone Substitutes: An Update. *Injury* **2005**, *36* (3), S20–S27. https://doi.org/10.1016/j.injury.2005.07.029.

(17) Wang, W.; Yeung, K. W. K. Bone Grafts and Biomaterials Substitutes for Bone Defect Repair: A Review. *Bioact. Mater.* **2017**, *2* (4), 224–247. https://doi.org/https://doi.org/10.1016/j.bioactmat.2017.05.007.

(18) Kurien, T.; Pearson, R. G.; Scammell, B. E. Bone Graft Substitutes Currently Available in Orthopaedic Practice: The Evidence for Their Use. *Bone Jt. J.* **2013**, *95 B* (5), 583–597. https://doi.org/10.1302/0301-620X.95B5.30286.

(19) Zwingenberger, S.; Nich, C.; Valladares, R. D.; Yao, Z.; Stiehler, M.; Goodman, S. B. Recommendations and Considerations for the Use of Biologics in Orthopedic Surgery. *BioDrugs* **2012**, *26* (4), 245–256. https://doi.org/10.2165/11631680-000000000-00000.

(20) Scheer, J. H.; Adolfsson, L. E. Tricalcium Phosphate Bone Substitute in Corrective Osteotomy of the Distal Radius. *Injury* **2009**, *40* (3), 262–267. https://doi.org/10.1016/j.injury.2008.08.013.

(21) Nich, C.; Sedel, L. Bone Substitution in Revision Hip Replacement. *Int. Orthop.* **2006**, *30* (6), 525–531. https://doi.org/10.1007/s00264-006-0135-6.

(22) Gaasbeek, R. D. A.; Toonen, H. G.; Van Heerwaarden, R. J.; Buma, P. Mechanism of Bone Incorporation of β-TCP Bone Substitute in Open Wedge Tibial Osteotomy in Patients. *Biomaterials* **2005**, *26* (33), 6713–6719. https://doi.org/10.1016/j.biomaterials.2005.04.056.

(23) Schwartz, C.; Bordei, R. Biphasic Phospho-Calcium Ceramics Used as Bone Substitutes Are Efficient in the Management of Severe Acetabular Bone Loss in Revision Total Hip Arthroplasties. *Eur. J. Orthop. Surg. Traumatol.* **2005**, *15* (3), 191–196. https://doi.org/10.1007/s00590-005-0244-8.

(24) Oonishi, H.; Iwaki, Y.; Kin, N.; Kushitani, S.; Murata, N.; Wakitani, S.; Imoto, K. Hydroxyapatite In Revision Of Total Hip Replacements With Massive Acetabular Defects: 4- To 10-Year Clinical Results. *J. Bone Jt. Surg.* **1997**, *79* (1), 87–92.

https://doi.org/10.1302/0301-620X.79B1.1290.

(25) Kargozar, S.; Baino, F.; Hamzehlou, S.; Hill, R. G.; Mozafari, M. Bioactive Glasses : Sprouting Angiogenesis in Tissue Engineering. *Trends Biotechnol.* **2017**, *xx*, 1–15. https://doi.org/10.1016/j.tibtech.2017.12.003.

(26) Hench, L. L.; Roki, N.; Fenn, M. B. Bioactive Glasses: Importance of Structure and Properties in Bone Regeneration. *J. Mol. Struct.* **2014**, *1073* (C), 24–30. https://doi.org/10.1016/j.molstruc.2014.03.066.

(27) Jones, J. R. Review of Bioactive Glass: From Hench to Hybrids. *Acta Biomater.* **2013**, *9*, 4457–4486. https://doi.org/10.1016/j.actbio.2015.07.019.

(28) Hench, L. L. The Story of Bioglass®. *J. Mater. Sci. Mater. Med.* **2006**, *17* (11), 967–978. https://doi.org/10.1007/s10856-006-0432-z.

(29) Hench, L. L.; Paschall, H. A. Direct Chemical Bond of Bioactive Glass-ceramic Materials to Bone and Muscle. *J. Biomed. Mater. Res.* **1973**, *7*, 25–42. https://doi.org/10.1002/jbm.820070304.

(30) Hench, L. L. Bioactive Materials for Gene Control. In *New Materials and Technologies for Healthcare*; IMPERIAL COLLEGE PRESS, 2011; pp 25–48. https://doi.org/doi:10.1142/9781848165595_0003.

(31) Li, Y.; Chen, S.; Li, L.; Qin, L. Bone Defect Animal Models for Testing Efficacy of Bone Substitute Biomaterials. **2015**. https://doi.org/10.1016/j.jot.2015.05.002.

(32) El-Rashidy, A. A.; Roether, J. A.; Harhaus, L.; Kneser, U.; Boccaccini, A. R. Regenerating Bone with Bioactive Glass Scaffolds: A Review of in Vivo Studies in Bone Defect Models. *Acta Biomater.* **2017**, *62*, 1–28. https://doi.org/10.1016/j.actbio.2017.08.030.

(33) Pearce, A. I.; Richards, R. G.; Milz, S.; Schneider, E.; Pearce, S. G. Animal Models for Implant Biomaterial Research in Bone: A Review. *Eur. Cells Mater.* **2007**, *13* (0), 1–10. https://doi.org/10.22203/eCM.v013a01.

(34) Augat, P.; Margevicius, K.; Simon, J.; Wolf, S.; Suger, G.; Claes, L. Local Tissue Properties in Bone Healing: Influence of Size and Stability of the Osteotomy Gap. *J. Orthop. Res.* **2005**, *16*, 475–481. https://doi.org/10.1002/jor.1100160413.

(35) Machado, C. P. G.; Sartoretto, S. C.; Alves, A. T. N. N.; Lima, I. B. C.; Rossi, A. M.; Granjeiro, J. M.; Calasans-Maia, M. D. Histomorphometric Evaluation of Strontium-Containing Nanostructured Hydroxyapatite as Bone Substitute in Sheep. *Braz. Oral Res.* **2016**, *30* (1), 1–11. https://doi.org/10.1590/1807-3107BOR-2016.vol30.0045.

(36) Li, J. J.; Akey, A.; Dunstan, C. R.; Vielreicher, M.; Friedrich, O.; Bell, D.; Zreiqat, H.

Effects of Material-Tissue Interactions on Bone Regeneration Outcomes Using Baghdadite Implants in a Large Animal Model. *Adv. Healthc. Mater.* **2018**, *1800218*, 1–9. https://doi.org/10.1002/adhm.201800218.

(37) Pobloth, A. M.; Johnson, K. A.; Schell, H.; Kolarczik, N.; Wulsten, D.; Duda, G. N.; Schmidt-Bleek, K. Establishment of a Preclinical Ovine Screening Model for the Investigation of Bone Tissue Engineering Strategies in Cancellous and Cortical Bone Defects. *BMC Musculoskelet. Disord.* **2016**, *17* (1), 1–12. https://doi.org/10.1186/s12891-016-0964-4.

(38) Muschler, G. F.; Raut, V. P.; Patterson, T. E.; Wenke, J. C.; Hollinger, J. O. The Design and Use of Animal Models for Translational Research in Bone Tissue Engineering and Regenerative Medicine. *Tissue Eng. Part B. Rev.* **2010**, *16* (1), 123–145. https://doi.org/10.1089/ten.TEB.2009.0658.

(39) Walsh, W. R.; Oliver, R. A.; Christou, C.; Lovric, V.; Walsh, E. R.; Prado, G. R.; Haider, T. Critical Size Bone Defect Healing Using Collagen-Calcium Phosphate Bone Graft Materials. *PLoS One* **2017**, *12* (1), 1–21. https://doi.org/10.1371/journal.pone.0168883.

(40) Sheikh, Z.; Abdallah, M. N.; Hanafi, A. A.; Misbahuddin, S.; Rashid, H.; Glogauer, M. Mechanisms of in Vivo Degradation and Resorption of Calcium Phosphate Based Biomaterials. *Materials (Basel).* **2015**, *8* (11), 7913–7925. https://doi.org/10.3390/ma8115430.

(41) Gauthier, O.; Müller, R.; Von Stechow, D.; Lamy, B.; Weiss, P.; Bouler, J. M.; Aguado, E.; Daculsi, G. In Vivo Bone Regeneration with Injectable Calcium Phosphate Biomaterial: A Three-Dimensional Micro-Computed Tomographic, Biomechanical and SEM Study. *Biomaterials* **2005**, *26* (27), 5444–5453. https://doi.org/10.1016/j.biomaterials.2005.01.072.

(42) Nazarian, A.; Müller, R. Time-Lapsed Microstructural Imaging of Bone Failure Behavior. *J. Biomech.* **2004**, *37* (1), 55–65. https://doi.org/10.1016/S0021-9290(03)00254-9.

(43) Tozzi, G.; Zhang, Q. H.; Tong, J. 3D Real-Time Micromechanical Compressive Behaviour of Bone-Cement Interface: Experimental and Finite Element Studies. *J. Biomech.* **2012**, *45* (2), 356–363. https://doi.org/10.1016/j.jbiomech.2011.10.011.

(44) Tozzi, G.; Danesi, V.; Palanca, M.; Cristofolini, L. Elastic Full-Field Strain Analysis and Microdamage Progression in the Vertebral Body from Digital Volume Correlation. *Strain* **2016**, *52* (5), 446–455. https://doi.org/10.1111/str.12202.

(45) Gillard, F.; Boardman, R.; Mavrogordato, M.; Hollis, D.; Sinclair, I.; Pierron, F.; Browne, M. The Application of Digital Volume Correlation (DVC) to Study the Microstructural Behaviour of Trabecular Bone during Compression. *J. Mech. Behav. Biomed. Mater.* **2014**, *29*, 480–499. https://doi.org/10.1016/j.jmbbm.2013.09.014.

(46) Liu, L.; Morgan, E. F. Accuracy and Precision of Digital Volume Correlation in Quantifying Displacements and Strains in Trabecular Bone. *J. Biomech.* **2007**, *40* (15), 3516–3520. https://doi.org/10.1016/j.jbiomech.2007.04.019.

(47) Tozzi, G.; Zhang, Q. H.; Tong, J. Microdamage Assessment of Bone-Cement Interfaces under Monotonic and Cyclic Compression. *J. Biomech.* **2014**, *47* (14), 3466–3474. https://doi.org/10.1016/j.jbiomech.2014.09.012.

(48) Danesi, V.; Tozzi, G.; Cristofolini, L. Application of Digital Volume Correlation to Study the Efficacy of Prophylactic Vertebral Augmentation. *Clin. Biomech.* **2016**, *39*, 14–24. https://doi.org/10.1016/j.clinbiomech.2016.07.010.

(49) Voide, R.; Schneider, P.; Stauber, M.; Wyss, P.; Stampanoni, M.; Sennhauser, U.; van Lenthe, G. H.; Müller, R. Time-Lapsed Assessment of Microcrack Initiation and Propagation in Murine Cortical Bone at Submicrometer Resolution. *Bone* **2009**, *45* (2), 164–173. https://doi.org/10.1016/j.bone.2009.04.248.

(50) Thurner, P. J.; Wyss, P.; Voide, R.; Stauber, M.; Stampanoni, M.; Sennhauser, U.; Müller, R. Time-Lapsed Investigation of Three-Dimensional Failure and Damage Accumulation in Trabecular Bone Using Synchrotron Light. *Bone* **2006**, *39* (2), 289–299. https://doi.org/10.1016/j.bone.2006.01.147.

(51) Christen, D.; Levchuk, A.; Schori, S.; Schneider, P.; Boyd, S. K.; Müller, R. Deformable Image Registration and 3D Strain Mapping for the Quantitative Assessment of Cortical Bone Microdamage. *J. Mech. Behav. Biomed. Mater.* **2012**, *8*, 184–193. https://doi.org/10.1016/j.jmbbm.2011.12.009.

(52) Dall'Ara, E.; Peña-Fernández, M.; Palanca, M.; Giorgi, M.; Cristofolini, L.; Tozzi, G. Precision of DVC Approaches for Strain Analysis in Bone Imaged with MCT at Different Dimensional Levels. *Front. Mater.* **2017**, *4:31*. https://doi.org/10.3389/fmats.2017.00031.

(53) Palanca, M.; Bodey, A. J.; Giorgi, M.; Viceconti, M.; Lacroix, D.; Cristofolini, L.; Dall'Ara, E. Local Displacement and Strain Uncertainties in Different Bone Types by Digital Volume Correlation of Synchrotron Microtomograms. *J. Biomech.* **2017**, *c*. https://doi.org/10.1016/j.jbiomech.2017.04.007.

(54) Comini, F.; Palanca, M.; Cristofolini, L.; Dall'Ara, E. Uncertainties of Synchrotron

MicroCT-Based DVC Bone Strain Measurements under Simulated Deformation. *J. Biomech.* **2018**.

(55) Peña Fernández, M.; Barber, A. H.; Blunn, G. W.; Tozzi, G. Optimisation of Digital Volume Correlation Computation in SR-MicroCT Images of Trabecular Bone and Bone-Biomaterial Systems. *J. Microsc.* **2018**, *00* (0), 1–16. https://doi.org/doi: 10.1111/jmi.12745.

(56) Coathup, M. J.; Edwards, T. C.; Samizadeh, S.; Lo, W. J.; Blunn, G. W. The Effect of an Alginate Carrier on Bone Formation in a Hydroxyapatite Scaffold. *J. Biomed. Mater. Res. - Part B Appl. Biomater.* **2016**, *104* (7), 1328–1335. https://doi.org/10.1002/jbm.b.33395.

(57) Vallet-Regi, M. *Bio-Ceramics with Clinical Applications*, 1st ed.; John Wiley & Sons, Incorporated, 2014.

(58) Wheeler, D. L.; Jenis, L. G.; Kovach, M. E.; Marini, J.; Turner, A. S. Efficacy of Silicated Calcium Phosphate Graft in Posterolateral Lumbar Fusion in Sheep. *Spine J.* **2007**, *7* (3), 308–317. https://doi.org/10.1016/j.spinee.2006.01.005.

(59) Sriranganathan, D.; Kanwal, N.; Hing, K. A.; Hill, R. G. Strontium Substituted Bioactive Glasses for Tissue Engineered Scaffolds : The Importance of Octacalcium Phosphate. *J. Mater. Sci. Mater. Med.* **2016**, *27* (2), 1–10. https://doi.org/10.1007/s10856-015-5653-6.

(60) Keaveny, T. M.; Borchers, R. E.; Gibson, L. J.; Hayes, W. C. Trabecular Bone Modulus and Strenght Can Depend on Specimen Geometry. *J. Biomech.* **1993**, *26* (8), 991–1000.

(61) Atwood, R. C.; Bodey, A. J.; Price, S. W. T.; Basham, M.; Drakopoulos, M. A High-Throughput System for High-Quality Tomographic Reconstruction of Large Datasets at Diamond Light Source. *Philos. Trans. R. Soc. A Math. Phys. Eng. Sci.* **2015**, *373* (2043). https://doi.org/10.1098/rsta.2014.0398.

(62) Peña Fernández, M.; Cipiccia, S.; Bodey, A. J.; Parwani, R.; Dall'Ara, E.; Blunn, G.; Pani, M.; Barber, A. H.; Tozzi, G. Effect of SR-MicroCT Exposure Time on the Mechanical Integrity of Trabecular Bone Using in Situ Mechanical Testing and Digital Volume Correlation. *J. Mech. Behav. Biomed. Mater.* **2018**, *88* (August), 109–119. https://doi.org/https://doi.org/10.1016/j.jmbbm.2018.08.012.

(63) Basham, M.; Filik, J.; Wharmby, M. T.; Chang, P. C. Y.; El Kassaby, B.; Gerring, M.; Aishima, J.; Levik, K.; Pulford, B. C. A.; Sikharulidze, I.; Sneddon, D.; Webber, M.; Dhesi, S. S.; Maccherozzi, F.; Svensson, O.; Brockhauser, S.; Náray, G., Ashton, A.

W. Data Analysis WorkbeNch (DAWN). *J. Synchrotron Radiat.* **2015**, *22*, 853–858. https://doi.org/10.1107/S1600577515002283.

(64) Titarenko;, V.; Bradley;, R.; Martin;, C.; Withers;, P. J.; Titarenko;, S. Regularization Methods for Inverse Problems in X-Ray Tomography. *Proc. SPIE 7804* **2010**, No. Developments in X-Ray Tomography VII. https://doi.org/doi: 10.1117/12.860260.

(65) Buades, A.; Coll, B.; Morel, J.-M. Non-Local Means Denoising. *Image Process. Line* **2011**, *1*, 490–530. https://doi.org/10.5201/ipol.2011.bcm_nlm.

(66) Darbon, J.; Cunha, A.; Chan, T. F.; Osher, S.; Jensen, G. J. Fast Nonlocal Filtering Applied to Electron Cryomicroscopy. *2008 5th IEEE Int. Symp. Biomed. Imaging from Nano to Macro, Proceedings, ISBI. IEEE* **2008**, 1331–1334. https://doi.org/10.1109/ISBI.2008.4541250.

(67) Palanca, M.; Tozzi, G.; Cristofolini, L.; Viceconti, M.; Dall'Ara, E. 3D Local Measurements of Bone Strain and Displacement: Comparison of Three Digital Volume Correlation Approaches. *J. Biomech. Eng.* **2015**, *137* (July), 1–14. https://doi.org/10.1115/1.4030174.

(68) Ford, C. M.; Keaveny, T. M. The Dependence of Shear Failure Properties of Trabecular Bone on Apparent Density and Trabecular Orientation. *J. Biomech.* **1996**, *29* (10), 1309–1317.

(69) Niebur, G. L.; Feldstein, M. J.; Yuen, J. C.; Chen, T. J.; Keaveny, T. M. High-Resolution Finite Element Models with Tissue Strength Asymmetry Accurately Predict Failure of Trabecular Bone. *J. Biomech.* **2000**, *33* (12), 1575–1583. https://doi.org/10.1016/S0021-9290(00)00149-4.

(70) Barth, H. D.; Launey, M. E.; MacDowell, A. A.; Ager, J. W.; Ritchie, R. O. On the Effect of X-Ray Irradiation on the Deformation and Fracture Behavior of Human Cortical Bone. *Bone* **2010**, *46* (6), 1475–1485. https://doi.org/10.1016/j.bone.2010.02.025.

(71) Bayraktar, H. H.; Morgan, E. F.; Niebur, G. L.; Morris, G. E.; Wong, E. K.; Keaveny, T. M. Comparison of the Elastic and Yield Properties of Human Femoral Trabecular and Cortical Bone Tissue. *J. Biomech.* **2004**, *37* (1), 27–35. https://doi.org/10.1016/S0021-9290(03)00257-4.

(72) Cristofolini, L. In Vitro Evidence of the Structural Optimization of the Human Skeletal Bones. *J. Biomech.* **2015**, *48* (5), 787–796. https://doi.org/10.1016/j.jbiomech.2014.12.010.

(73) Jungmann, R.; Szabo, M. E.; Schitter, G.; Yue-Sing Tang, R.; Vashishth, D.; Hansma,

P. K.; Thurner, P. J. Local Strain and Damage Mapping in Single Trabeculae during Three-Point Bending Tests. *J. Mech. Behav. Biomed. Mater.* **2011**, *4* (4), 523–534. https://doi.org/10.1016/j.jmbbm.2010.12.009.

(74) Luczynski, K. W.; Steiger-Thirsfeld, A.; Bernardi, J.; Eberhardsteiner, J.; Hellmich, C. Extracellular Bone Matrix Exhibits Hardening Elastoplasticity and More than Double Cortical Strength: Evidence from Homogeneous Compression of Non-Tapered Single Micron-Sized Pillars Welded to a Rigid Substrate. *J. Mech. Behav. Biomed. Mater.* **2015**, *52*, 51–62. https://doi.org/https://doi.org/10.1016/j.jmbbm.2015.03.001.

(75) Schwiedrzik, J.; Raghavan, R.; Bürki, A.; LeNader, V.; Wolfram, U.; Michler, J.; Zysset, P. In Situ Micropillar Compression Reveals Superior Strength and Ductility but an Absence of Damage in Lamellar Bone. *Nat. Mater.* **2014**, *13*, 740.

(76) Goodheart, J. R.; Miller, M. A.; Mann, K. A. In Vivo Loss of Cement-Bone Interlock Reduces Fixation Strength in Total Knee Arthroplasties. *J. Orthop. Res.* **2014**, *32* (8), 1052–1060. https://doi.org/10.1002/jor.22634.

(77) Coathup, M.; Smith, N.; Kingsley, C.; Buckland, T.; Dattani, R.; Ascroft, G. P.; Blunn, G. Impaction Grafting with a Bone-Graft Substitute in a Sheep Model of Revision Hip Replacement. *J. Bone Jt. Surg. - Br. Vol.* **2008**, *90–B* (2), 246–253. https://doi.org/10.1302/0301-620X.90B2.19675.

(78) Wang, P.; Zhao, L.; Liu, J.; Weir, M. D.; Zhou, X.; Xu, H. H. K. Bone Tissue Engineering via Nanostructured Calcium Phosphate Biomaterials and Stem Cells. *Bone Res.* **2015**, *2* (July). https://doi.org/10.1038/boneres.2014.17.

(79) Coathup, M. J.; Hing, K. A.; Samizadeh, S.; Chan, O.; Fang, Y. S.; Campion, C.; Buckland, T.; Blunn, G. W. Effect of Increased Strut Porosity of Calcium Phosphate Bone Graft Substitute Biomaterials on Osteoinduction. *J. Biomed. Mater. Res. - Part A* **2012**, *100 A* (6), 1550–1555. https://doi.org/10.1002/jbm.a.34094.

(80) Bodey, A. J.; Rau, C. Launch of the I13-2 Data Beamline at the Diamond Light Source Synchrotron. *J. Phys. Conf. Ser.* **2017**, *849* (1). https://doi.org/10.1088/1742-6596/849/1/012038.

For Table of Contents Use Only

Full-field strain analysis of bone-biomaterial systems produced by the implantation of osteoregenerative biomaterials in an ovine model

Marta Peña Fernández[1], Enrico Dall'Ara[2], Andrew J. Bodey[3], Rachna Parwani[1], Asa H. Barber[1,4], Gordon W. Blunn[5], Gianluca Tozzi[1]*